

# Influence of container shape on scaling of turbulent fluctuations in convection

N. Foroozani,<sup>1,2</sup> J. J. Niemela,<sup>1</sup> V. Armenio,<sup>2</sup> and K. R. Sreenivasan<sup>3</sup>

<sup>1</sup>*International Centre for Theoretical Physics, Strada Costiera, 11, 34151 Trieste, Italy*

<sup>2</sup>*Dipartimento di Ingegneria e Architettura, Università di Trieste, P.le Europa 1, 34100 Trieste, Italy*

<sup>3</sup>*Departments of Physics and Mechanical Engineering, and the Courant Institute of Mathematical Sciences, New York University, New York, New York 10012, USA*

(Received 31 July 2014; published 8 December 2014)

We perform large-eddy simulations of turbulent convection in a cubic cell for Rayleigh numbers,  $Ra$ , between  $10^6$  and  $10^{10}$  and the molecular Prandtl number,  $Pr = 0.7$ . The simulations were carried out using a second-order-accurate finite-difference method in which subgrid-scale fluxes of momentum and heat were both parametrized using a Lagrangian and dynamic Smagorinsky model. The scaling of the root-mean-square fluctuations of density (temperature) and velocity measured in the cell center are in excellent agreement with the scaling measured in the laboratory experiments of Daya and Ecke [*Phys. Rev. Lett.* **87**, 184501 (2001)] and differ substantially from that observed in cylindrical cells. We also observe the *time-averaged* spatial distributions of the local heat flux and density fluctuations, and find that they are strongly inhomogeneous in the horizontal midplane, with the largest density gradients occurring at the corners at the midheight, where hot and cold plumes mix in the form of strong counter-rotating eddies.

DOI: 10.1103/PhysRevE.90.063003

PACS number(s): 47.27.te, 47.20.Bp, 47.27.ep

Turbulent Rayleigh-Bénard convection (RBC) in a fluid heated from below is a challenging problem in nonlinear physics, with many important applications in natural and engineering systems. Because of the complexity of the governing equations, analytical progress in understanding convection has been slow, and laboratory experiments and numerical simulations have assumed increased importance. In regard to numerical work, large-eddy-simulation (LES) techniques have proved their value as reliable tools for investigating large-scale quantities as well as flow topology and structure [1]. In the present work, we use LES to shed light on a previously reported experimental result [2]—henceforth DE01—that the scaling of turbulent fluctuations in the geometric center of the convection cell are strongly influenced by the *geometrical shape* of the convection cell, and confirm its validity.

The lateral *confinement* of turbulent convection can indeed influence the global flow properties for width-to-height aspect ratios  $\Gamma$  close to unity, because of the presence of a large-scale circulation (LSC), or “mean wind,” which encompasses the entire cell [3]; but it was unexpected prior to DE01 that the cross-sectional geometrical shape can have significant effect on the scaling of fluctuations. In this work, in addition to repeating the experiment of DE01 numerically, we also investigate the mean and fluctuating velocity, heat flux, and the mean wind to shed light on physical processes occurring in a cubic cell that could explain the different statistics. It is known that the LSC in a cell with a square cross section arranges itself in a diagonal plane, pinned to one diagonal set of the corners [4,5]. This pinning does not happen in cylindrical cells, at least in the absence of mechanisms such as tilting that break rotational symmetry, where the LSC has complete azimuthal freedom [6]. Correspondingly, we find substantial spatial inhomogeneity in fluctuations over long times in the cubic cell.

In RBC flows the principal control parameter is the Rayleigh number,  $Ra \equiv \alpha \Delta T g H^3 / \nu \kappa$ . Here  $g$  is the gravitational acceleration,  $\alpha$ ,  $\nu$ , and  $\kappa$  are, respectively, the thermal expansion coefficient, kinematic viscosity, and thermal diffusivity of the fluid, and  $\Delta T$  is the vertical temperature difference

across the fluid layer of height  $H$ . Other control parameters include the Prandtl number  $Pr = \nu/\kappa$  and geometric parameters of the confinement, which include the aspect ratio  $\Gamma$ . An important measured quantity in response to forcing is the global transport of heat along the mean (vertical) gradient of temperature, which is represented by the nondimensional heat transport (the Nusselt number); it depends strongly on  $Ra$  and weakly on  $Pr$  and presumably also on geometric features.

In DE01 the authors used a cell whose height was 70% of the length of the sides ( $\Gamma = 0.7$ ). The working fluid was water, with  $Pr = 5.46$ . For our simulations we chose a cubic geometry ( $\Gamma = 1$ ) and  $Pr = 0.7$  in order to allow comparison to other reference data from direct numerical simulations (DNS). Neither of these differences from DE01 are significant for present discussions, and our result simply reinforces the idea that shape plays the critical role in determining the scaling of fluctuations. We cover the Rayleigh number range from  $10^6$  to  $10^{10}$ , which is a larger range (both lower and higher ends of  $Ra$ ) than that of DE01.

As already stated, the numerical simulation methodology used is LES where the large scales are simulated while the subgrid (SGS) scales are parametrized. The LES methodology has been validated against DNS in Rayleigh-Bénard convection [1] for the case of two infinite and parallel plates in the range  $6.3 \times 10^5 < Ra < 1 \times 10^8$ , obtaining an excellent agreement for the first- and second-order statistics. Further below we will compare our heat transfer results with recent DNS work.

We solve the spatially filtered Boussinesq approximation of the unsteady Navier-Stokes equations in 3D:

$$\frac{\partial \bar{u}_j}{\partial x_j} = 0, \quad (1)$$

$$\frac{\partial \bar{u}_i}{\partial t} + \frac{\partial \bar{u}_j \bar{u}_i}{\partial x_j} = -\frac{1}{\rho_0} \frac{\partial \bar{P}}{\partial x_i} + \nu \frac{\partial^2 \bar{u}_i}{\partial x_j \partial x_j} - \frac{\bar{\rho}}{\rho_0} g \delta_{i2} - \frac{\partial \tau_{ij}}{\partial x_j}, \quad (2)$$

$$\frac{\partial \bar{\rho}}{\partial t} + \frac{\partial \bar{u}_j \bar{\rho}}{\partial x_j} = k \frac{\partial^2 \bar{\rho}}{\partial x_j \partial x_j} - \frac{\partial \lambda_j}{\partial x_j}, \quad (3)$$

where  $x_1, x_2, x_3$  denote the three spatial coordinates with  $x_2$  as the vertical (upward) direction,  $u_i$  is the velocity component in the  $x_i$  direction,  $P$  is pressure, and  $\delta_{ij}$  is the Kronecker symbol. In the model it is assumed that density  $\rho$  depends linearly on temperature as  $\rho = \rho_0[1 - \alpha(T - T_0)]$ , where  $\rho_0$  is the density at the reference temperature  $T_0$ . The overbar symbol denotes the filtering operation which is performed here in the physical space using a top-hat filter function. The effect of the unresolved small scales appears through the terms  $\tau_{ij} = \overline{u_i u_j} - \overline{u_i} \overline{u_j}$  and  $\lambda_j = \overline{u_j \rho} - \overline{u_j} \overline{\rho}$  in the momentum and density equations, respectively. We use a dynamic eddy viscosity model to parametrize the SGS momentum and buoyancy fluxes as described in [7]. The model is treated according to the Lagrangian technique of [8].

We apply the no-slip condition on all six walls. The vertical lateral walls are perfectly adiabatic  $[(\partial \overline{\rho} / \partial \mathbf{n}) = 0]$ , where  $\mathbf{n}$  is the normal vector] and the top and bottom walls are isothermal with a fixed temperature difference  $\Delta T$  giving a density difference  $\Delta \rho$ . We vary the Rayleigh number between  $10^6$  and  $10^{10}$ .

In all simulations the grid spacing is finer in the regions close to the walls in order to resolve properly the momentum and the thermal boundary layers. We use  $32 \times 64 \times 32$  ( $\approx 6.5 \times 10^4$ ) grid cells in  $x, y, z$  directions, respectively, for  $10^6 \leq Ra \leq 10^8$  and increase the resolution to  $64 \times 96 \times 64$  for higher  $Ra$ . Note that our resolution is coarser than that given by the  $N \sim Re_f^{9/5}$  criterion of [9] ( $\approx 4.5 \times 10^6$  for  $Ra = 10^8$ ) established for DNS, where  $N$  denotes the number of grid points. However, for all  $Ra$  we verified that the number of grid points in the thermal boundary layer ( $N_{BL}$ ) was larger than 3, exceeding the criterion of Verzicco and Camussi [10]. The velocity is made nondimensional with the free-fall velocity  $U_f = \sqrt{(g\alpha\Delta TH)}$ . We then find that  $Ra/Pr = U_f^2 H^2 / \nu^2 = Re_f^2$ , where  $Re_f$  is the Reynolds number based on  $U_f$ . A characteristic time scale is the free-fall time  $t_f = H/U_f$  [11–14]. In all the numerical runs, data sampling started once the flow was fully turbulent and had become statistically steady. Moreover, individual runs were performed for over  $5000t_f$ , which is an order of magnitude larger than that typically used in DNS (see, e.g., [11]).

The Nusselt number ( $Nu$ ) is a response to the input parameters  $Ra$ ,  $Pr$ , and  $\Gamma$  and is defined here as

$$Nu = \frac{\kappa \partial_y \langle \rho \rangle_{A,t} - \langle u_y \rho \rangle_{A,t}}{\kappa \Delta \rho H^{-1}}, \quad (4)$$

where  $\langle \dots \rangle_{A,t}$  denotes averaging over horizontal planes and time. The two contributions in the numerator of Eq. (4) are due to the diffusive and turbulent heat fluxes. Note that in this specific flow the Nusselt number is constant along the vertical, and equal to that at the top or bottom walls. In order to verify the accuracy of the basic quantities obtained in our simulations, we compare our results with those of [11] who used DNS (Table I).

Overall, the Nusselt number obtained from our simulations is in excellent agreement with the DNS data, being only 1.8% or so higher. The slightly higher  $Nu$  for higher values of  $Ra$  can be attributed to insufficient thermal dissipation close to the sidewall, so that hot plumes can travel further from the bottom (top) plate than in simulations (see [14]). In terms of its scaling

TABLE I. Computational parameters and heat transport data for cubic cavities and for  $Pr = 0.7$  and varying  $Ra$ . The number of grid points in the  $i$  direction is given by  $N_i$ .  $N_{BL}$  denotes the number of points in the thermal boundary layer; included for comparison are the DNS data on heat transport [11] for the same values of  $Ra$ .

$Ra$	$N_x \times N_y \times N_z$	$N_{BL}$	$Nu$	$Nu_{Ref. [11]}$
$1 \times 10^6$	$32 \times 64 \times 32$	14	8.31	8.32
$3 \times 10^6$	$32 \times 64 \times 32$	11	11.4	11.5
$1 \times 10^7$	$32 \times 64 \times 32$	10	16.4	16.3
$3 \times 10^7$	$32 \times 64 \times 32$	8	22.4	22.0
$1 \times 10^8$	$32 \times 64 \times 32$	6	31.6	31.3
$1 \times 10^9$	$64 \times 96 \times 64$	5	63.4	
$1 \times 10^{10}$	$64 \times 96 \times 64$	5	116.2	

with  $Ra$  we obtained  $Nu = 0.15Ra^{0.29}$ , in good agreement with  $Nu = 0.19Ra^{0.28 \pm 0.1}$ , the experimental result in the cubic cell of [5] using water as the working fluid.

Figure 1 illustrates the time-averaged streamlines for  $Ra = 10^6$ . The flow exhibits a mean wind moving along one diagonal [Fig. 1(a)] with two small recirculation regions in the corners: one is at the top-left corner of the figure where the mean wind coming from below impinges the upper surface of the cavity and the other is at the lower-right corner where the descending mean wind impinges the bottom surface. In the opposite diagonal [Fig. 1(b)] two strong counter-rotating vortex structures are shown converging at the midplane. Such counter-rotating flows have also been observed in other simulations (see, e.g., [11]). This complex flow structure has significant effects on the resulting turbulent fields.

The mean wind depicted in Fig. 1 influences the spatial distribution of local heat flux within the thermal boundary layers. We calculate local nondimensional vertical heat flux at the bottom and top plates as

$$Nu_w(x, z) = \frac{H}{\Delta \rho} \frac{\partial \langle \rho(x, z) \rangle_t}{\partial y} \Big|_w. \quad (5)$$

In Fig. 2, the spatial distribution of the *heat flux inhomogeneity* on the top and bottom plates,  $Nu_w/Nu$ , is presented along with velocity vectors at the first grid points from the wall. The mean wind, oriented along one diagonal plane of the cube, governs the spatial distribution of the heat flux at the wall, which is

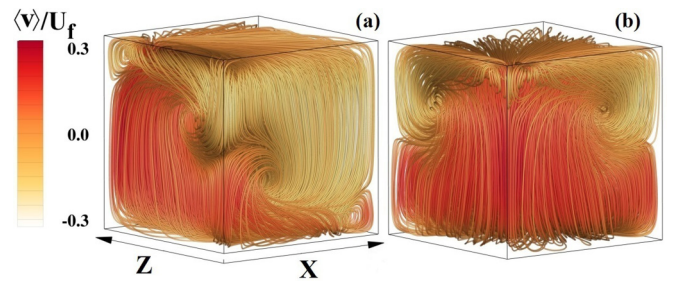


FIG. 1. (Color online) Streamlines within the full convection cell, time averaged for more than  $5296t_f$ . Gray scale (color online) denotes the intensity of the vertical mean velocity, normalized by the free-fall velocity scale  $U_f$ . Figure (a) shows the diagonal containing the mean wind and (b) shows the opposite diagonal, containing the strong, counter-rotating cells.  $Ra = 10^6$ ;  $Pr = 0.7$ ;  $\Gamma = 1$ .

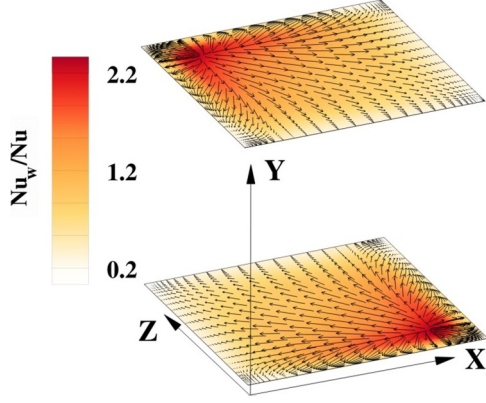


FIG. 2. (Color online) Contour plots of local heat flux  $Nu_w$  at the top and bottom plates, time averaged over  $5296t_f$ . Gray scale (color online) gives the magnitude of the local heat flux in units of the global Nusselt number. Velocity vectors show the diagonal direction of the LSC for clarity.  $Ra = 10^6$ ;  $Pr = 0.7$ ;  $\Gamma = 1$ .

strongly inhomogeneous over horizontal planes in steady state. The heat flux at the corner, where the flow impinges on the wall, is much larger than that at the center and on opposite corners. Figure 1 also shows that the mean flow exhibits symmetry with respect to the diagonal plane containing the LSC.

The statistics of density and velocity fluctuations in the cell center are our next focus. We define the root-mean-square (rms) of the resolved density fluctuations as  $\sigma_\rho(\mathbf{x}) = [\langle \rho(\mathbf{x})\rho(\mathbf{x}) \rangle_t - \langle \rho(\mathbf{x}) \rangle_t \langle \rho(\mathbf{x}) \rangle_t]^{1/2}$ , and that of resolved vertical velocity fluctuations as  $\sigma_v(\mathbf{x}) = [\langle v(\mathbf{x})v(\mathbf{x}) \rangle_t - \langle v(\mathbf{x}) \rangle_t \langle v(\mathbf{x}) \rangle_t]^{1/2}$ . The SGS contribution to the rms is negligible. The normalized density and velocity fluctuations are shown in Fig. 3 as functions of  $Ra$ .

The measured fluctuations of density,  $\sigma_\rho/\Delta\rho$ , are well described at the cell center by the power law  $\sigma_\rho/\Delta\rho = 49.03Ra^{-0.46}$  (solid line). The scaling behavior is in excellent agreement with DE01 for a near-cubic cell with  $\Gamma = 0.7$ ,  $Pr = 5.46$ . Indeed, those authors found a power exponent of  $-0.48 \pm 0.03$  [the dashed line in Fig. 3(a)] while, for cylindrical cells under the same experimental conditions, they measured the considerably smaller exponent of  $-0.1 \pm 0.02$  (the dash-dotted line). In Fig. 3(b) we show the rms velocity fluctuations in our cubic cell and fit it by  $\sigma_v H/\nu = 0.31Ra^{0.39}$ . This result is also in good agreement with DE01 in which the measured exponent was  $0.36 \pm 0.05$  (dashed line). By way of contrast, their result for cylindrical cell, shown again by a dashed-dotted line, demonstrates the large difference resulting from the change in cross-sectional geometry. The data in Fig. 3 were taken at the cell center. It thus appears reasonable to state that the strong variation between the results for near-cubic or cubic containers, on the one hand, and those for cylindrical containers, on the other, may be tied to “fixed” inhomogeneities of the fluctuation field in the case of the former. The time-averaged mapping of density fluctuations shown in Fig. 4 reveals fixed inhomogeneities in the vertical planes corresponding to the two diagonals. At the midheight level, the higher levels of *rms* density fluctuations correspond to the diagonal opposite that of the LSC where we observe strong counter-rotating vortex structures [see Fig. 1(b)] which mix hot and cold plumes at their midheight convergence. Thus

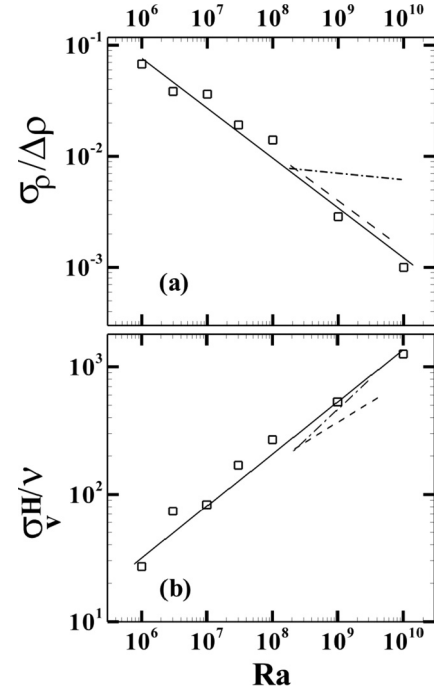


FIG. 3. Normalized fluctuations in (a) density, given by  $\sigma_\rho/\Delta\rho$  and (b) vertical velocity, given by  $\sigma_v H/\nu$ , measured at the cell center. The solid lines are the power-law fits to the present data:  $\sigma_\rho/\Delta\rho = 49.03Ra^{-0.46}$  (top) and  $\sigma_v H/\nu = 0.31Ra^{0.39}$  (bottom). Dashed and dash-dotted lines are power-law fits, respectively, for the near-cubic cell and cylindrical cell of DE01 for comparison.

it is no surprise that the largest gradient in density fluctuations occurs there. These counter-rotating flows provide a steady source for the time-averaged horizontal gradient in rms density fluctuations in the central horizontal plane, which provides a physical mechanism for the observed difference in scaling of fluctuations at the cell center between square or cylindrical cross sections in steady state and under long-time averaging.

In conclusion, we have performed numerical simulations of turbulent Rayleigh-Bénard convection in a fluid confined within a cubic enclosure and with molecular Prandtl number

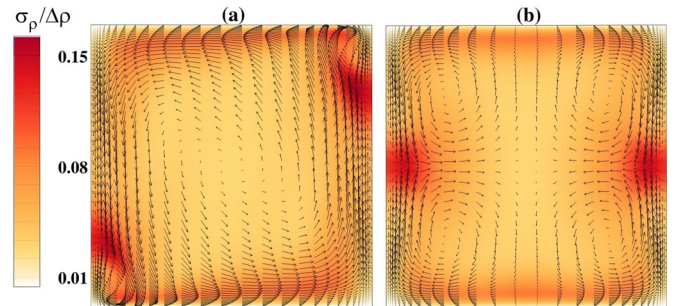


FIG. 4. (Color online) Time-averaged values of the rms density fluctuations  $\sigma_\rho$ . Gray scale (color online) denotes the magnitude of the density fluctuations in units of  $\Delta\rho$ . Averaging has been performed over  $5296t_f$ . Figure (a) shows the vertical diagonal plane containing the large-scale circulation and (b) the orthogonal plane to it containing the counter-rotating cells. We have included the velocity vectors for clarity.  $Ra = 10^6$ ;  $Pr = 0.7$ ;  $\Gamma = 1$ .

0.7. Data sampling started only after the flow was turbulent and had attained steady-state conditions. We observed a stable pattern of LSC for all  $Ra$  investigated. Extending the range of  $Ra$  accessed by DE01, we have confirmed the scaling seen by those authors for both density (temperature) and velocity fluctuations at the cell center and provide insights on physical mechanisms for the observed scaling properties. We point out that  $Pr$  and  $\Gamma$  are slightly different in the experiment as compared to the simulation, which serves to reinforce the conjecture that cross-sectional geometry (shape) rather than aspect ratio or Prandtl number is the most significant factor in

determining the scaling exponent of *rms* fluctuations at the cell center. The time-averaged, spatial distribution of velocity and its fluctuations provides a key to understanding the differences in scaling observed in cylindrical cells—which in principle have rotational symmetry—to cubic or near-cubic cells which do not.

The authors acknowledge valuable discussions with M. Kaczorowski and B. Geurts. The simulations have been run on the ARGO supercomputer of the International Centre for Theoretical Physics, Trieste, Italy.

- 
- [1] S. J. Kimmel and J. A. Domaradzki, *Phys. Fluids* **12**, 169 (2000).
  - [2] Z. A. Daya and R. E. Ecke, *Phys. Rev. Lett.* **87**, 184501 (2001).
  - [3] J. J. Niemela, L. Skrbek, K. R. Sreenivasan, and R. J. Donnelly, *J. Fluid Mech.* **449**, 169 (2001).
  - [4] M. Sano, X. Z. Wu, and A. Libchaber, *Phys. Rev. A* **40**, 6421 (1989).
  - [5] X.-L. Qiu and K.-Q. Xia, *Phys. Rev. E* **58**, 486 (1998).
  - [6] E. Brown and G. Ahlers, *Phys. Rev. Lett.* **98**, 134501 (2007).
  - [7] V. Armenio and S. Sarkar, *J. Fluid Mech.* **459**, 1 (2002).
  - [8] C. Meneveau, T. S. Lund, and W. H. Cabot, *J. Fluid Mech.* **319**, 353 (1996).
  - [9] H. Choi and P. Moin, *Phys. Fluids* **24**, 011702 (2012).
  - [10] R. Verzicco and R. Camussi, *J. Fluid Mech.* **477**, 19 (2003).
  - [11] M. Kaczorowski and K. Q. Xia, *J. Fluid Mech.* **722**, 596 (2013).
  - [12] S. Grossmann and D. Lohse, *Phys. Fluids* **16**, 4462 (2004).
  - [13] F. Chillà and J. Schumacher, *Eur. Phys. J. E* **35**, 58 (2012).
  - [14] G. Amati, K. Koal, F. Massaioli, K. R. Sreenivasan, and R. Verzicco, *Phys. Fluids* **17**, 121701 (2005).